Efficiency and Physical Limitations of Adiabatic Direct Energy Conversion in Axisymmetric Fields

J.-M. Rax*
Andlinger Center for Energy and Environment, Princeton University, Princeton, New Jersey 08544, USA and IJCLab, Université de Paris-Saclay, 91405 Orsay, France

E.J. Kolmes† and N.J. Fisch
Department of Astrophysical Sciences, Princeton University, Princeton, New Jersey 08544, USA

(Received 20 October 2024; revised 22 January 2025; accepted 29 January 2025; published 20 February 2025)

We describe and analyze a new class of direct energy conversion schemes based on the adiabatic magnetic drift of charged particles in axisymmetric magnetic fields. The efficiency of conversion as well as the geometrical and dynamical limitations of the recoverable power are calculated. The geometries of these axisymmetric field configurations are suited for direct energy conversion in radiating advanced aneutronic reactors and in advanced divertors of deuterium-tritium tokamak reactors. The $\mathbf{E} \times \mathbf{B}$ configurations considered here do not suffer from the classical drawbacks and limitations of thermionic and magnetohydrodynamic high-temperature direct energy conversion devices.

DOI: 10.1103/PRXEnergy.4.013007

I. INTRODUCTION

Part of the internal energy content of a thermodynamical system can be extracted to produce useful work. Under reversible extraction conditions, the allowed maximum extracted work is given by the free energy difference between the initial and final states [1,2]. The *free energy content* of a system is always lower than its total *internal energy content*. Their difference is proportional to the temperature and the entropy, which are always positive. Moreover, entropy production due to irreversible operations decreases the fraction of the internal energy that can be converted into useful work.

Energy conversion underlies many of the technologies that have been proposed to decarbonize the world's energy infrastructure. In addition to economic and environmental considerations, the efficiency of free energy extraction is one of the most important factors determining the relative merits of different technologies [3].

Thermodynamical energy conversion systems are usually based on simple nonequilibrium states displaying gradients of intensive variables. The most common thermodymamical nonequilibrium states used as free energy sources in classical conversion devices involve (1) pressure, (2) temperature, and (3) chemical potential gradients [4]. Pressure gradients can be relaxed in turbines to produce mechanical work with a high conversion efficiency. Steady-state free energy extraction associated with a simple temperature differential is limited by the Carnot reversible efficiency at zero power and by the Curzon-Alborn-Novikov-Chambadal endoreversible efficiency at maximum power [5–7]. This type of endoreversible model takes into account the entropy production associated with (1) the heat flux from the hot source (temperature T_h) to the engine and (2) the heat flux from the engine to the cold source (temperature T_c). This lowers the efficiency from the classical Carnot value $1 - T_c/T_h$ down to $1 - \sqrt{T_c/T_h}$. Chemical potential differences can be efficiently converted in electrochemical devices but are, unfortunately, usually relaxed through open air combustion to sustain a temperature gradient in combustion-driven systems.

Besides classical thermal conversion schemes, direct energy conversion (DEC) schemes such as magnetohydrodynamic (MHD) generators, thermionic (TI) diodes, photovoltaic (PV) cells, and redox (RX) cells of the hydrogen type have been recognized to offer the potential of significant conversion efficiency as they avoid the inefficient steps requiring the cooling or heating of a compressed or expanded gas [8–10]. The basic principles of a dc electric power DEC generator are illustrated in Fig. 1(a). Two steps are required: free charge generation at a rate dN/dt followed by charge separation with a force $\pm F$ on positive and negative particles. The resulting flow of current must be oriented such that it provides power to an electric field E

*Contact author: jean-marcel.rax@universite-paris-saclay.fr
†Contact author: ekolmes@princeton.edu

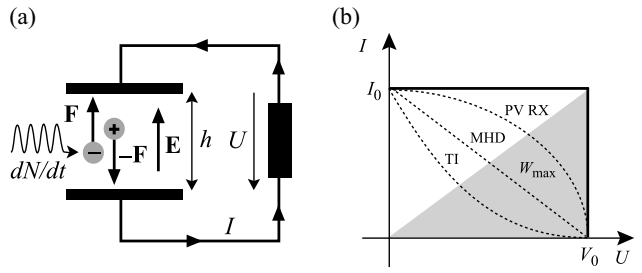

FIG. 1. (a) Basic layout of a dc electric power DEC generator. (b) Ideal and nonideal current-voltage characteristics (represented by the solid and dashed curves, respectively). In the ideal case, the generator can run at the same maximum current I_0 for any voltage up to V_0. In the nonideal case, that current performance tends to drop off as the voltage increases.

sustained between two electrodes separated by a gap width h.

A device's current-voltage (I-U) characteristic describes how its efficiency changes as its power throughput increases. Two conventions are sometimes used when currents and voltages are illustrated: (1) the receptor convention and (2) the generator convention. The choice of convention determines whether the current is drawn from high voltage to low voltage or vice versa. The latter convention is used in the figures in this paper. Under ideal operations, the current-voltage "square" characteristic of this ideal DEC generator is illustrated in Fig. 1(b). The short-circuit current I_0 is given by

$$I_0 = 2q\frac{dN}{dt}, \tag{1}$$

where q is the single-particle charge. The open-circuit voltage

$$V_0 = \frac{Fh}{q} \tag{2}$$

is reached when the electric force $\pm qE = \pm qU/h$ balances the separating force $\pm F$.

When nonideal processes are taken into account the "square" ideal characteristic becomes either a curve of the concave (TI) or convex (PV and RX) type, or simply a resistive straight line (MHD), depicted by the three dotted curves in Fig. 1(b) [8]. The maximum power W_{max} that can be delivered to the external load from an ideal generator is given by

$$W_{max} = I_0 U_0/2 = Fh\,(dN/dt)\,. \tag{3}$$

The force F used in DEC devices is typically of a statistical nature: thermodynamical forces associated with the gradient of an intensive variable such as pressure, temperature, or chemical potential. In the new class of plasma DEC presented and analyzed here, the force F is the centrifugal force due to the curvature of the magnetic field lines and the diamagnetic force due to the gradient of the magnetic field strength. These are thermal forces because their effects are proportional to the kinetic/thermal energy of the particles. This kinetic/thermal energy can be transformed into dc electric power through the design of a dedicated field configuration.

One of the main problems of plasma-based DEC generators is the ultimate collection of the free charges. The heating of the anode in TI diodes and the erosion of the electrodes in MHD devices have been widely studied [9], and tungsten plates provide the optimal choice. The principle of plasma DEC described here offers the advantage that the configuration can be designed to slow down the charged particles to a very low energy so that secondary emission on the anode (collecting electrons) and sputtering on the cathode (collecting ions) can be minimized, as can heating. Nevertheless, even with this advantage the use of tungsten plates remains the best choice. We will not address the engineering issue of the optimal electrode material in greater detail, as this paper is devoted to the presentation of the basic principles.

We now briefly review the principles of the classical plasma-based DEC generators. In TI diodes, F is associated with the pressure/temperature gradient of the free electrons emitted by the hot cathode. Ions remain bound in the cathode lattice and sustain a phonon gas rather than flowing. In MHD generators, F is the friction force of the flowing neutral part of the weakly ionized plasma. In PV generators, F is a chemical potential gradient resulting from the chemical potential difference between the two sides of the PV junction.

The type of DEC generator illustrated in Fig. 1(a) is well suited when the separating force F acts in opposite directions on electrons and ions. If the force F is insensitive to the sign of the charges, we can either immobilize one type of particle or use an $\mathbf{E}\times\mathbf{B}$ configuration where the $\mathbf{F}\times\mathbf{B}/qB^2$ drift velocity separates the charges. An ideal $\mathbf{E}\times\mathbf{B}$ configuration is illustrated in Fig. 2. For a

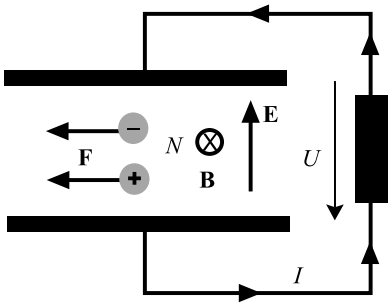

FIG. 2. An illustration of an ($\mathbf{E}\times\mathbf{B}$)-type configuration. A force $\mathbf{F}$ acts similarly on both positive and negative charged particles, so the resulting $\mathbf{F}\times\mathbf{B}$ drifts separate the charges.

small voltage drop U and a steady-state population of $2N$ charged particles in the electrode gap, the ideal power W_0 of the generator is the product of the drift velocity F/qB and the electric force qE:

$$W_0 = 2NFE/B. \tag{4}$$

The past decades witnessed the massive development of PV and RX cell DEC generators, which are now produced on a fully developed industrial scale. The performances of high-temperature TI and MHD DEC generators remain below the requirement to envision an industrial-scale development. Despite the lack of industrial-scale achievements, the continuous interest in TI and MHD systems stems from the fact that they operate at high temperatures: (1) for a given amount of energy, high-temperature heat offers the potential of a far better conversion than low-temperature heat; (2) for the same power, high-temperature MHD and TI systems occupy a smaller footprint than classical systems.

Very high temperature heat is produced in thermonuclear reactors, (1) in the form of a high-temperature plasma flow at the level of the divertor in ^{2}H-^{3}H tokamak reactors or (2) in the form of high-intensity short-wavelength radiation in advanced neutronless p-^{11}B reactors. An efficient high-temperature DEC scheme would be very beneficial for ^{2}H-^{3}H and p-^{11}B fusion schemes. Several processes have been proposed to achieve direct conversion of thermonuclear energy [11], such as cusp configurations [12], traveling waves [13], and advanced electrostatic configurations [14,15] or electrostatic and magnetostatic configurations of the $\mathbf{E} \times \mathbf{B}$ type [16]. In this work we analyze a class of high-temperature DEC schemes of the $\mathbf{E} \times \mathbf{B}$ type free from the usual drawbacks of MHD and TI devices. The drawbacks of high-temperature TI and MHD DEC devices have been known for a long time; for instance, the occurrence of space charge-limited flow in vacuum TI diodes and the erosion of the edge electrodes in MHD generators put severe restrictions on the efficiency of such generators.

For example, we consider the thermionic diode illustrated in Fig. 3(a). A high-temperature source sustains a temperature difference between a hot cathode (T_c) and a cold anode ($T_a \ll T_c$). Thermionic emission, described by the Richardson-Dushman law [17], occurs at the inner surface of the cathode, and electrons, with mass m, work against an electric field E during their transit from the cathode toward the anode.

Under optimal conditions, the voltage U of such an electric generator is given by the relation $mv^2 = 2qU$, where $v \sim \sqrt{k_B T_c/m}$ is the average emission velocity. However, the heat-driven current I is limited by the Child-Langmuir law, limiting the current density J_{CL} (amperes per square meter) to a value given by

$$J_{\mathrm{CL}} = 2\varepsilon_0 m v^3/9qh^2, \tag{5}$$

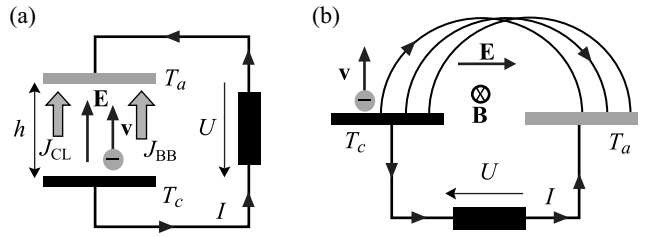

FIG. 3. Two thermionic diode configurations: (a) the basic configuration, in which thermionic emission ejects electrons parallel to an electric field, and (b) a modified configuration, in which a magnetic field is used to avoid the Child-Langmuir and blackbody limitations on the attainable current.

where h is the anode-cathode gap width. Thus, to extract significant power, an impractically tiny gap is needed. Moreover, besides the electron flux described by J_{CL}, the blackbody flux of photons J_{BB} (watts per square meter) provides a thermal short circuit dramatically lowering the conversion efficiency when h is small,

$$J_{\mathrm{BB}} = \pi^2 k_B^4 T_c^4/15\hbar^3 c^2, \tag{6}$$

where $\hbar$ is Planck's constant. To avoid these drawbacks, an $\mathbf{E} \times \mathbf{B}$ configuration, illustrated in Fig. 3(b), has been proposed [18]. The current across the magnetic field B is no longer limited to J_{CL}, and J_{BB} no longer heats up the cold anode, but the ballistic coupling between the cathode and the anode is inefficient because of the dispersion in the velocities of the electrons. Other mitigations of the TI drawbacks, such as the use of plasma TI diodes rather than vacuum TI diodes [19], have been considered, but none of them have made it possible to achieve the expected high conversion efficiency.

Nevertheless, $\mathbf{E} \times \mathbf{B}$ configurations have proven their usefulness in MHD generator designs used to convert the free enthalpy of a hot weakly ionized plasma flow into dc electric power. This $\mathbf{E} \times \mathbf{B}$ configuration is illustrated in Fig. 4(a). A weakly ionized plasma flows, with velocity $\mathbf{v}$ along the x axis, across a magnetic field $\mathbf{B}$ directed

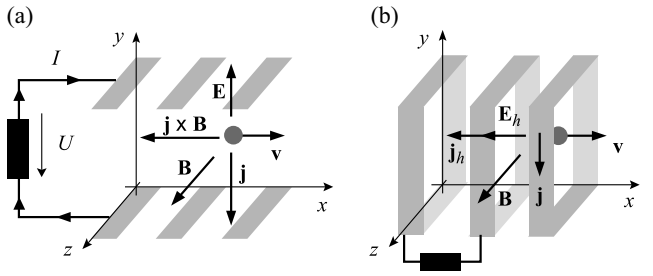

FIG. 4. Two MHD generator configurations: (a) the Faraday configuration and (b) the Hall configuration. In both cases, the system generates an electric field (and current) by directing a flow perpendicular to a magnetic field. Note the appearance of Hall currents as a result.

along the z axis [20]. Electrons and ions set up a current $\mathbf{j}$ under the influence of the $\mathbf{v} \times \mathbf{B}$ force. This current provides power to the electric field $\mathbf{E}$ along the y axis. Energy conservation is ensured as the $\mathbf{j} \times \mathbf{B}$ force slows down the flow along the x axis. The short-circuiting of the y currents provides another $\mathbf{E} \times \mathbf{B}$ configuration besides the segmented Faraday configuration illustrated in Fig. 4(a): the Hall configuration illustrated in Fig. 4(b). The basic physical principles and main limitations of Faraday and Hall MHD DEC generators can be found in textbooks [21,22]. Despite the simplicity and effectiveness of the physical principles put to work in Faraday and Hall generators, the management of a hot weakly ionized collisional plasma flow has proven to be difficult, and MHD generators have not found their way to industrial development up to now.

The use of $\mathbf{E} \times \mathbf{B}$ configurations aimed at DEC is not restricted to the advanced TI and classical MHD generators illustrated in Figs. 3 and 4. We describe and analyze in this paper another $\mathbf{E} \times \mathbf{B}$ configuration, where the thermal energy of charged particles is converted to a dc electromotive force in very particular types of inhomogeneous magnetic and electric fields.

This configuration does not suffer from the major drawbacks of the TI scheme and the MHD scheme. The Child-Langmuir law limitation does not apply, and electrode erosion is minimized as the charged particles strike the electrodes at low energy. This configuration also has its own advantages: (1) the energy extraction rate is exponential with respect to time and (2) the closed field line topology minimizes plasma losses. Besides the topology, the geometry is particularly pertinent for high-temperature conversion in fusion reactors. The proposed configuration can be understood as a way of converting plasma kinetic energy into electricity. It can also be understood as a technique for capturing radiation, if that radiation is used to ionize neutrals and the energy is captured from the resulting charged particles.

This paper is organized as follows. In the next section we describe the way to arrange coils and electrode plates in poloidal and toroidal axisymmetric configurations to extract the thermal energy of a plasma. We analyze the energy exchange between charged particles and the electric field that provides the electromotive force of the generator in these $\mathbf{E} \times \mathbf{B}$ configurations in Secs. III and IV. We calculate the efficiency and the irreducible physical limitations on the power delivered by toroidal DEC generator in Secs. V and VI. We do not consider the limitations associated with the stress on the material in a high-temperature environment. This paper is instead devoted to an analysis of the physical principles. The adaptation of these DEC scheme to ^{2}H-^{3}H tokamak reactors and p-^{11}B advanced reactors is briefly considered in Sec. VII. The last section summarizes our new results and gives our conclusions.

II. E × B COOLING IN POLOIDAL AND TOROIDAL CONFIGURATIONS

The design of a hot plasma DEC device requires the identification of a structure such that the motion of the charged particles is slowed down by an electric field sustained between two electrodes. As a result of global energy conservation, this $\mathbf{E} \times \mathbf{B}$ electric cooling of a hot plasma results in the sustainment of an electromotive force when the electrode circuit is closed on an external load.

The magnetic drift velocity is proportional to $\mathbf{B} \times \nabla B$ and to the thermal energy content of the plasma particles. The sign of the resulting power transfer between the hot plasma and the electric field is controlled by the sign of the dot product of the drift velocity and the electric field. The condition for plasma cooling and dc power generation is

$$\mathbf{E} \cdot \mathbf{B} \times \nabla B < 0. \tag{7}$$

This can be adjusted in axisymmetric magnetic field configurations through the electrode plates' P positions, shapes, and polarizations, so plasma cooling and electric power generation can be envisioned and are studied in the next sections. In the axisymmetric magnetic field configurations depicted in Figs. 5(a) and 6(a), the charged particle motion is the drift motion in an inhomogeneous magnetic field and the electric field is sustained between electrode plates P collecting the drift current $\mathbf{J}$. The azimuthal angle around the Cartesian axis z is denoted by θ ($0 \leq \theta < 2\pi$), and the unit vector $\mathbf{e}_\theta$ corresponds to this azimuthal direction. Any axisymmetric magnetic field $\mathbf{B}$ can be represented as the sum of a poloidal field and a toroidal field: $\mathbf{B} = B_T \mathbf{e}_\theta + \nabla \times (A_P \mathbf{e}_\theta)$, where the first term on the right-hand side is the toroidal component and the second is the poloidal component. Thus, we consider two types of structure aimed at extracting the free energy of a hot plasma and converting it into dc electric power: toroidal and poloidal configurations illustrated, respectively, in Figs. 5 and 6. For toroidal generators, the electric field is axial, and for poloidal generators, the electric field is azimuthal.

In Fig. 5(b), the $z =$ const ring-shaped conducting electrodes P are used to collect the drift current $\mathbf{J}$ in the axial direction. In Fig. 6(b), the $\theta =$ const plane electrodes P are used to collect the drift current $\mathbf{J}$ in the azimuthal direction. With these orientations of the electric and magnetic fields, the adiabatic magnetic drift velocity of the hot charged particles can be directed against the electric field's force to extract thermal energy and cool down the plasma. In both cases, this drift current $\mathbf{J}$ provides dc power $\mathbf{J} \cdot \mathbf{E}$ to the external load.

A complete analysis must also take into account the electric $\mathbf{E} \times \mathbf{B}/B^2$ drift. We will see that the impact of this drift is to facilitate energy conversion at low values of E and inhibit it at larger values.

An axisymmetric vacuum magnetic field, $\nabla \times \mathbf{B} = \mathbf{0}$, $\nabla \cdot \mathbf{B} = 0$, $\partial \mathbf{B}/\partial\theta = \mathbf{0}$, either poloidal or toroidal, is

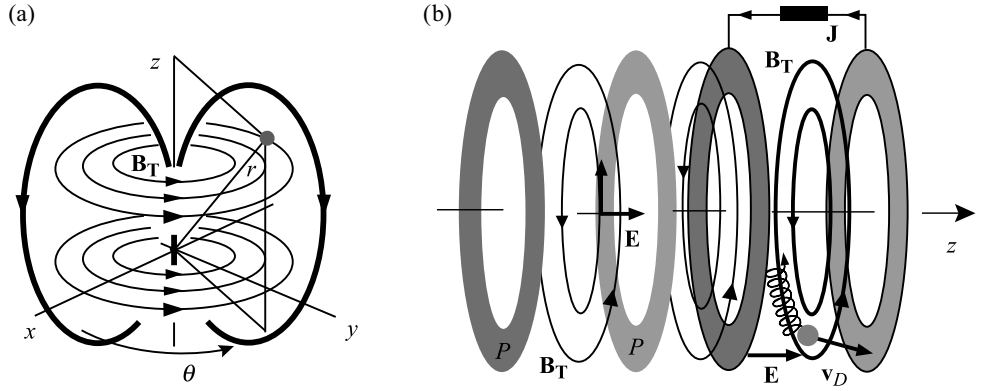

FIG. 5. A toroidal field configuration for DEC. (a) The positioning of the coils (bold external loops) used to generate the magnetic field $\mathbf{B}_T$. (b) The current-collecting electrode plates P that generate the electric field $\mathbf{E}$. $\mathbf{v}_D$ is the drift velocity, which is the source of the drift current $\mathbf{J}$.

locally represented on the Frenet-Serret basis associated with the magnetic field line as $\mathbf{B} = B\mathbf{b}$. The gradient ∇B includes two terms

$$\nabla B = \frac{\partial B}{\partial s}\mathbf{b} + \frac{B}{R}\mathbf{n}, \tag{8}$$

where R is the curvature radius of the field line, s is the curvilinear abscissa along the field line, and $\mathbf{b} = B/B$ and $\mathbf{n} = \partial\mathbf{b}/\partial s$ are the unit tangent and normal vectors to the field line: the Frenet-Serret moving frame without torsion. The $\mathbf{b}$ component in Eq. (8) generates the diamagnetic force along the field lines, and the $\mathbf{n}$ component generates the drift velocity.

In Sec. III, toroidal magnetic fields are conveniently described with a cylindrical set of coordinates $[r, \theta, z]$ rather than with the Cartesian one $[x, y, z]$ ($x = r\cos\theta, y = r\sin\theta$). The toroidal magnetic field, displayed in Fig. 5(b), is assumed to be without ripple despite the finite number of coils C,

$$\mathbf{B} = B\mathbf{e}_\theta = B_0\frac{r_0}{r}\mathbf{e}_\theta, \tag{9}$$

$$\mathbf{E} = -\nabla\phi = -E\mathbf{e}_z, \tag{10}$$

where r_0, E, and B_0 are positive constants. Here we have used Ampère's theorem, $Br = B_0 r_0$, and introduced the electric potential ϕ. The gradient of the magnetic field strength is directed along the radial direction:

$$\nabla B = -\frac{B}{r}\mathbf{e}_r. \tag{11}$$

For a purely toroidal field $\mathbf{n} = -\mathbf{e}_r$, $\partial B/\partial s = 0$, and $R = r$. The poloidal magnetic field configuration illustrated in

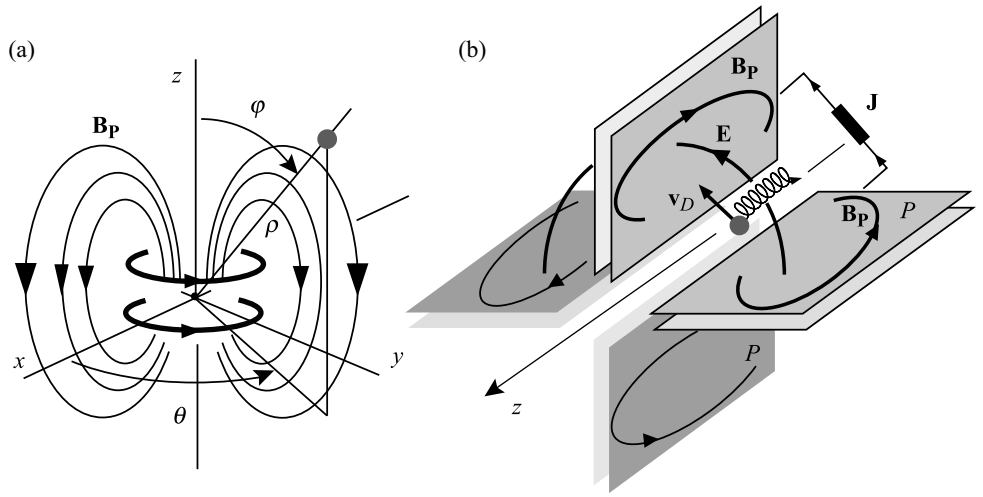

FIG. 6. A poloidal field configuration for DEC. (a) The positioning of the magnetic field coils (bold internal loops) used to generate the magnetic field $\mathbf{B}_P$. (b) The electrode plates P that generate the electric field $\mathbf{E}$. $\mathbf{v}_D$ is the drift velocity, which is the source of the drift current $\mathbf{J}$.

Fig. 6 and analyzed in Sec. IV is usually described with spherical coordinates $[\rho, \varphi, \theta]$ rather than cylindrical coordinates $[r, \theta, z]$ ($r = \rho \sin\varphi$, $z = \rho \cos\varphi$). The azimuthal electric field depicted in Fig. 6(b) can be approximated by

$$\mathbf{E} = -E\mathbf{e}_\theta = -\nabla\phi. \tag{12}$$

The full expression for the field from the electrodes in Fig. 6(b) would include some additional terms, but the simple form given in Eq. (12) is sufficient to show the essential behavior of the energy transfer mechanism. For the poloidal case, we assume (1) that the source of the thermal plasma is restricted to the region near the equatorial plane $\varphi \approx \pi/2$ in between each pair of plates and (2) that the field geometry and the conducting electrode plates P are designed such that the capture of the positive and negative charges, above and below this equatorial plane, occurs at a small angle φ. It is convenient to consider the Frenet-Serret representation [Eq. (8)], in which the radius of curvature of the field lines is denoted by R and the gradient scale length L along the field line is defined as $B/L = \partial B/\partial s$. Along a given field line, both the radius R and the length L are functions of s, and we describe the gradient of the magnetic field in the drift region, above and below the equatorial plane, along and across the field lines between the electrodes, with the model

$$\nabla B = \frac{B}{L}\mathbf{b} + \frac{B}{R}\mathbf{n}, \tag{13}$$

where rather than the exact functions $L(s)$ and $R(s)$, we consider the average over s of $L(s)$ and $R(s)$ in the region explored by the charged particles in between the equatorial plane and the ultimate capture by the electrodes P at a small angle φ. This approximation makes it simpler to show the dependence of the conversion process on R and L in cases where both are important.

III. ADIABATIC THERMAL ENERGY CONVERSION IN TOROIDAL FIELDS

Consider a cylindrical set of coordinates $[R, \theta, z]$ associated with the cylindrical basis $[\mathbf{e}_r, \mathbf{e}_\theta, \mathbf{e}_z]$. The position of a particle with charge q and mass m is given by $R\mathbf{e}_r(\theta) + z\mathbf{e}_z$. The field geometry between two electrodes is illustrated in Fig. 7. We calculate the thermal energy extraction resulting from the drift-driven electric cooling. The $\mathbf{E} \times \mathbf{B}$ configuration (Fig. 7) is described by Eqs. (9) and (10), where we take $r = R$.

The gradient of the azimuthal magnetic field strength is radial and is described by Eq. (11):

$$\nabla B = -B_0 \frac{R_0}{R^2}\mathbf{e}_r = -\frac{B}{R}\mathbf{e}_r. \tag{14}$$

The motion of a charged particle in such a toroidal field configuration is a combination of a translation $v_\parallel$ along the magnetic field lines, cyclotron rotation $v_\perp$ around the field lines, and drift $\mathbf{v}_D$ across the magnetic field lines. The total velocity $\mathbf{v}$ is thus given by

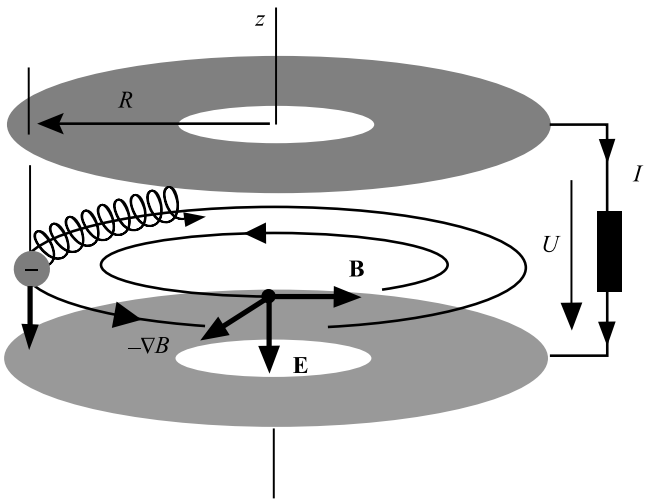

FIG. 7. The fields associated with a toroidal field, including the magnetic field strength gradient and the positions of the current-collecting electrodes.

$$\mathbf{v} = v_\parallel \frac{\mathbf{B}}{B} + \mathbf{v}_D + v_\perp \cos(\omega_c t)\,\mathbf{e}_r + v_\perp \sin(\omega_c t)\,\mathbf{e}_z, \tag{15}$$

where $\omega_c = qB/m$ is the cyclotron frequency. The drift velocity $\mathbf{v}_D$ is a combination of the magnetic and electric drifts:

$$\mathbf{v}_D = \frac{2\varepsilon_\parallel + \varepsilon_\perp}{qB^3}\mathbf{B} \times \nabla B + \frac{\mathbf{E} \times \mathbf{B}}{B^2}, \tag{16}$$

where we have introduced $\varepsilon_\parallel = mv_\parallel^2/2$, the kinetic energy along the field lines, and $\varepsilon_\perp = mv_\perp^2/2$, the cyclotron kinetic energy around the field lines. The axial and radial drift equations are given by

$$\frac{dz}{dt} = \frac{2\varepsilon_\parallel + \varepsilon_\perp}{qB^3}\mathbf{B} \times \nabla B \cdot \mathbf{e}_z, \tag{17}$$

$$\frac{dR}{dt} = \frac{\mathbf{E} \times \mathbf{B}}{B^2} \cdot \mathbf{e}_r. \tag{18}$$

The power transfer between the thermal energy and the electric energy is given by the dot product

$$q\mathbf{E} \cdot \mathbf{v}_D = \frac{2\varepsilon_\parallel + \varepsilon_\perp}{B^3}\mathbf{B} \times \nabla B \cdot \mathbf{E} = -\frac{2\varepsilon_\parallel + \varepsilon_\perp}{\tau}, \tag{19}$$

where we have introduced the secular timescale $\tau > 0$ defined as

$$\tau \doteq \left|\frac{B^3}{\mathbf{E} \times \mathbf{B} \cdot \nabla B}\right| = \frac{B_0 R_0}{E}. \tag{20}$$

The potential energy $q\phi = qEz$ increases in time at the expense of the thermal energy $\varepsilon_\parallel + \varepsilon_\perp$, so the sum of the kinetic energy and the potential energy ε remains constant. Two invariants can be identified: the magnetic moment μ is an adiabatic invariant and the energy ε is a Noether invariant. The cyclotron and total energies can be written as

$$\varepsilon_\perp(R) = \mu B(R), \tag{21}$$

$$\varepsilon(z,R) = \varepsilon_\parallel + \varepsilon_\perp + q\phi(z). \tag{22}$$

We have used the adiabatic ordering and ignored the small drift kinetic energy. The case of a strong electric field, where we take this drift energy into account, is considered in Sec. VI. Thus, as $d\mu/dt = 0$ and $d\varepsilon/dt = 0$, the adiabatic evolution of the energy is described by

$$\frac{d\varepsilon_\perp}{dt} = \left[\left(\mathbf{v}_D + v_\parallel \frac{\mathbf{B}}{B}\right)\cdot\nabla\right]\mu B, \tag{23}$$

$$\frac{d\varepsilon_\parallel}{dt} = -\left[\left(\mathbf{v}_D + v_\parallel \frac{\mathbf{B}}{B}\right)\cdot\nabla\right](q\phi + \mu B). \tag{24}$$

We consider here the slow evolution averaged over the fast cyclotron motion and we have eliminated $\varepsilon_\perp$ to set up Eq. (24) as $d\varepsilon/dt = 0$. The secular velocity operator involved in Eqs. (23) and (24) is given by

$$\left(\mathbf{v}_D + v_\parallel \frac{\mathbf{B}}{B}\right)\cdot\nabla = \frac{2\varepsilon_\parallel + \varepsilon_\perp}{qRB}\frac{\partial}{\partial z} + \frac{E}{B}\frac{\partial}{\partial R}, \tag{25}$$

where we note that the $v_\parallel$ term drops out due to axisymmetry. We substitute this secular velocity given in Eq. (25) into Eqs. (23) and (24) to get the thermal energy extraction dynamical equations

$$\frac{d\varepsilon_\parallel}{dt} = -2\frac{\varepsilon_\parallel}{\tau}, \tag{26}$$

$$\frac{d\varepsilon_\perp}{dt} = -\frac{\varepsilon_\perp}{\tau}. \tag{27}$$

We recover the energy balance from Eq. (19).

During the transit of one charged particle toward the electrode, its thermal energy decreases at an exponential rate with respect to time. This behavior provides an efficient way to directly extract the thermal energy. The physics behind this exponential extraction of the thermal energy

$$\varepsilon_\parallel + \varepsilon_\perp = \varepsilon_{\parallel 0}\exp\left(-\frac{2t}{\tau}\right) + \varepsilon_{\perp 0}\exp\left(-\frac{t}{\tau}\right) \tag{28}$$

can be described as follows.

The electric drift E/B is radial and pushes particles toward the lower-B region, where $\varepsilon_\perp = \mu B$ is converted into $\varepsilon_\parallel$ to ensure the adiabatic invariance of μ. At the very same time, the magnetic drift is axial along the z axis and pushes particles toward high-potential $q\phi$ regions, where $\varepsilon_\parallel + \varepsilon_\perp$ decreases to ensure the invariance of $\varepsilon = \varepsilon_\parallel + \varepsilon_\perp + q\phi$. This thermal energy extraction is illustrated in Fig. 8.

The drift equations given by Eqs. (17) and (18) can be integrated to give

$$z = z_0 + \frac{\varepsilon_{\parallel 0}}{qE}\left[1 - \exp\left(-\frac{2t}{\tau}\right)\right] + \frac{\varepsilon_{\perp 0}}{qE}\left[1 - \exp\left(-\frac{t}{\tau}\right)\right] \tag{29}$$

and

$$R = R_0\exp\left(\frac{t}{\tau}\right). \tag{30}$$

These two expressions determine the dimensions of a device needed to access a given extraction efficiency. These relations describe an expansion of the hot plasma and they set limitations on the full thermal energy extraction as the device must display a finite size and footprint. These geometrical limitations are analyzed in Sec. V.

IV. ADIABATIC THERMAL ENERGY CONVERSION IN POLOIDAL FIELDS

Before addressing the geometrical and dynamical limitations of the conversion efficiency of the process described by Eq. (28), we explore in this section the main difference between plasma cooling in a toroidal field and plasma cooling in a poloidal field. With the use of the model poloidal field described by Eqs. (12) and (13), Eqs. (26) and (27) describing adiabatic slowing down become

$$\frac{d\varepsilon_\parallel}{dt} = -2\frac{\varepsilon_\parallel}{\tau} - v_\parallel\frac{\varepsilon_\perp}{L}, \tag{31}$$

$$\frac{d\varepsilon_\perp}{dt} = -\frac{\varepsilon_\perp}{\tau} + v_\parallel\frac{\varepsilon_\perp}{L}. \tag{32}$$

We recover the general energy balance from Eq. (19), which is independent of the configuration, poloidal, toroidal, or mixed, although, in general, τ may become a function of s. Compared with Eqs. (26) and (27), there is an additional term due to the diamagnetic mirror force redistributing the energy between the parallel degree of freedom and cyclotron degree of freedom to ensure adiabatic invariance of μ. As opposed to the previous toroidal case, where the energy relations given by Eqs. (26) and (27) are exact in a perfect toroidal field, the poloidal case here is analyzed only on the basis of the approximate model poloidal field

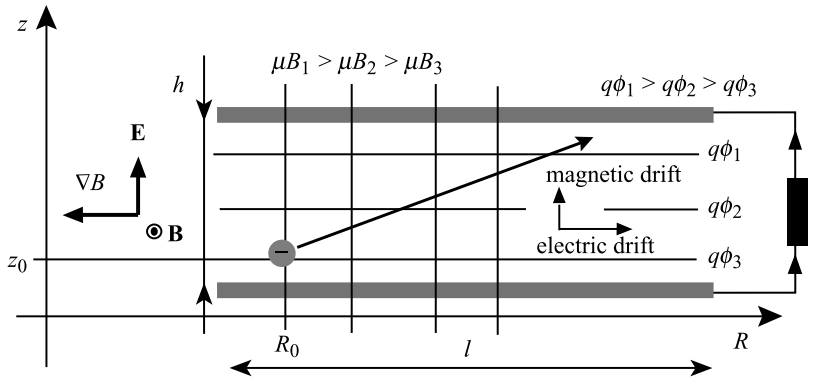

FIG. 8. The trajectory of a particle as it moves between the electrodes includes both magnetic and electric drift motion.

[Eq. (13)]. The aim of this section is to identify the impact of a gradient along the field lines.

The additional term L is treated as a small perturbation so that the zero-order solutions are just the solutions of Eqs. (26) and (27), which fulfills the conservation relation

$$\varepsilon_\perp/\sqrt{\varepsilon_\parallel} = \varepsilon_{\perp 0}/\sqrt{\varepsilon_{\parallel 0}}. \tag{33}$$

We introduce the characteristic time

$$\tau_0 = \frac{L}{\varepsilon_{\perp 0}}\sqrt{2m\varepsilon_{\parallel 0}}$$

and assume that $\tau < \tau_0$. Within the framework of this perturbative expansion, the cooling of the parallel energy [Eq. (31)] becomes

$$\frac{d\varepsilon_\parallel}{dt} = -2\frac{\varepsilon_\parallel}{\tau} \pm 2\frac{\varepsilon_\parallel}{\tau_0}. \tag{34}$$

The analysis of the cooling/conversion process occurs in the $(\varepsilon_\parallel, \varepsilon_\perp)$ energy space. In the toroidal case, the *cooling trajectories* in energy space, Eqs. (26) and (27), are all restricted to parabolic curves in this space:

$$\frac{d\varepsilon_\parallel}{\varepsilon_\parallel} = 2\frac{d\varepsilon_\perp}{\varepsilon_\perp}. \tag{35}$$

The interesting new phenomenon associated with the occurrence of a gradient of the field strength along the field line (L) is the possibility to shape different cooling trajectories according to

$$\frac{d\varepsilon_\parallel}{\varepsilon_\parallel\,(1/\tau \mp 1/\tau_0)} = 2\frac{d\varepsilon_\perp}{\varepsilon_\perp\left(1/\tau \pm 2\varepsilon_\perp\varepsilon_{\parallel 0}/\varepsilon_{\perp 0}^2\tau_0\right)}. \tag{36}$$

This new freedom opens the way to an optimization of the final stage of the free energy extraction. The necessity of such an optimization is clearly displayed by the analysis of the evolution of the anisotropy of the particle energy distribution function. Consider a particle with initial parallel, perpendicular, and total energies $\varepsilon_{\parallel 0}$, $\varepsilon_{\perp 0}$, and ε_0, respectively. Define the initial pitch angle ϑ by

$$\varepsilon_{\parallel 0} = \varepsilon_0 \cos^2\vartheta, \tag{37}$$

$$\varepsilon_{\perp 0} = \varepsilon_0 \sin^2\vartheta. \tag{38}$$

This gives $\varepsilon_{\parallel 0} + \varepsilon_{\perp 0} = \varepsilon_0$ by construction. Equipartition of energy between the three directions of motion corresponds to $\vartheta_{\rm EP} = \arccos(\sqrt{1/3})$. For the previous toroidal case, we found

$$\frac{\varepsilon_\perp}{\varepsilon_\parallel} = \tan^2\vartheta \exp\left(\frac{t}{\tau}\right). \tag{39}$$

This increase of the cyclotron energy at the expense of the parallel energy can be controlled if we modulate the purely toroidal field and introduce a new structural freedom with $L(s)$ continuously redistributing the cyclotron energy into the parallel energy during the slowing down process. This study of the optimization of the configuration of the magnetic and electric fields is left for future work as it must be addressed after a careful assessment of the limitations of the purely toroidal configuration. Sections V and VI are devoted to the analysis of these limitations, which are of dynamical and geometrical nature.

V. EFFICIENCY: GEOMETRICAL LIMITATIONS

We can define the efficiency of free energy extraction as the fraction $\eta \leq 1$ of extracted initial thermal energy

$$\eta = 1 - \frac{\varepsilon_\parallel(t) + \varepsilon_\perp(t)}{\varepsilon_0} \tag{40}$$

$$= 1 - \cos^2\vartheta \exp\left(-\frac{2t}{\tau}\right) - \sin^2\vartheta \exp\left(-\frac{t}{\tau}\right). \tag{41}$$

This relation clearly displays the advantage of the possibility to control, independently of the energy dynamics, the

dynamics of the pitch angle ϑ. Such a possibility is offered by a gradient of the field strength along the field line (L) analyzed in Sec. IV. One major limit on the achievable efficiency η is the time available before a particle strikes a boundary of the device. Following Fig. 8, let h be the width of the gap between the two electrodes and ℓ be the radial extent of the circular electrodes.

The transit from the inner edge $R = R_0$ to the outer edge $R = R_0 + \ell$ takes time t_r given by

$$\frac{t_r}{\tau} = \ln\left(1 + \frac{\ell}{R_0}\right). \tag{42}$$

A particle could also strike the axial boundary first. The time to transit from $z = z_0$ to $z = z_0 + h$ is given by

$$\frac{t_z}{\tau} = \ln \frac{\sin^2\vartheta + \sqrt{\sin^4\vartheta + 4\cos^2\vartheta\,(1 - qEh/\varepsilon_0)}}{2\,(1 - qEh/\varepsilon_0)}, \tag{43}$$

where Eh is the full voltage drop between the electrodes and qEh/ε_0 is the ratio of that potential energy to the initial kinetic energy of the particle. Note that the square root is real when $\varepsilon_0 > qEh$. Then this first limit is determined by the efficiency η that can be achieved in the lesser of t_r and t_z (or, in the case where $t_z \notin \mathbb{R}$, it is determined by t_r alone).

This can also be understood as a constraint on the system size required to achieve a particular efficiency η. Consider, for example, the case in which the radial size ℓ is limiting (rather than the axial size h). If $\vartheta = \vartheta_{\mathrm{EP}}$, ℓ and η are related by

$$\frac{\ell}{R_0} = \left(\sqrt{4 - 3\eta} - 1\right)^{-1} - 1. \tag{44}$$

Near-perfect efficiencies would require $\ell \gg R_0$. The axial gap h must also be large enough to ensure a significant conversion efficiency η, and our taking $h = z - z_0$ in Eq. (29) and a thermal distribution with equipartition gives the relation

$$\frac{qEh}{k_B T} = 3/2 - \left(\sqrt{4 - 3\eta} - 1\right)^2/2 - \left(\sqrt{4 - 3\eta} - 1\right). \tag{45}$$

Apart from the geometrical scaling, the other main constraint on this DEC scheme concerns the validity of the first-order adiabatic drift theory, which is analyzed in the next section.

VI. EFFICIENCY: DYNAMICAL LIMITATIONS

To identify the dynamical limit, we consider the next-order drift within the framework of adiabatic theory: the second-order inertial drift $\mathbf{v}_{\mathrm{DI}}$, which can be written as follows:

$$\mathbf{v}_{\mathrm{DI}} = \frac{\mathbf{B}}{qB^2} \times m\frac{d}{dt}\left(\frac{\mathbf{E}\times\mathbf{B}}{B^2}\right) = \frac{m}{qB\tau}\frac{\mathbf{E}}{B}. \tag{46}$$

Here τ is the same timescale as introduced in Eq. (20). We recognize here the usual polarization drift associated with the time variation τ. We see that this inertial drift is always along $q\mathbf{E}$ in the direction opposite the magnetic drift and provides a limiting effect on the previous first-order conversion process. This second-order drift does not affect the secular radial dynamics given in Eq. (18), but the secular axial dynamics in Eq. (17) becomes

$$\frac{dz}{dt} = (\mathbf{v}_D + \mathbf{v}_{\mathrm{DI}}) \cdot \mathbf{e}_z = \frac{2\varepsilon_\parallel + \varepsilon_\perp}{qE\tau} - \frac{mE}{qB^2\tau}. \tag{47}$$

For any given particle, the transfer of energy from kinetic energy to the electric field will reverse when $dz/dt = 0$, at which point ($z - z_0 = h^*$, $R = R_0 + l^*$) the device will operate no longer as a DEC generator but as an accelerator for that particle. In the following we define and calculate t^* as the time needed to reach this reversal point (h^*, l^*). An estimate of (h^*, l^*) can be obtained from Eqs. (29) and (30) evaluated at $t = t^*$. A more precise value can be obtained from the integration of the dynamical equations to be studied in this section. However, it turns out that the discussion of the efficiency limitation requires only the evaluation of t^*. This reversal of the energy transfer is illustrated in Fig. 9.

The power transfer between the thermal energy and the electric energy is given by the dot product $q\mathbf{E} \cdot (\mathbf{v}_D + \mathbf{v}_{\mathrm{DI}})$:

$$qE\frac{dz}{dt} = \frac{2\varepsilon_\parallel + \varepsilon_\perp}{\tau} - \frac{mE^2/B^2}{\tau}. \tag{48}$$

We define the drift energy as

$$\varepsilon_{E/B} = \frac{m}{2}\frac{E^2}{B^2}. \tag{49}$$

To study the limitation associated with this reversal of the energy transfer, we now consider the case in which the $\mathbf{E}\times\mathbf{B}$ drift may contain a significant fraction of the kinetic energy, in which case the leading-order expression for energy becomes

$$\varepsilon\,(z, R) = \varepsilon_\parallel + \varepsilon_\perp + \varepsilon_{E/B} + q\phi \tag{50}$$

rather than Eq. (22). The leading-order expression for energy conservation ought to be

$$\frac{d}{dt}\left(\varepsilon_\parallel + \mu B + q\phi + \varepsilon_{E/B}\right) = 0. \tag{51}$$

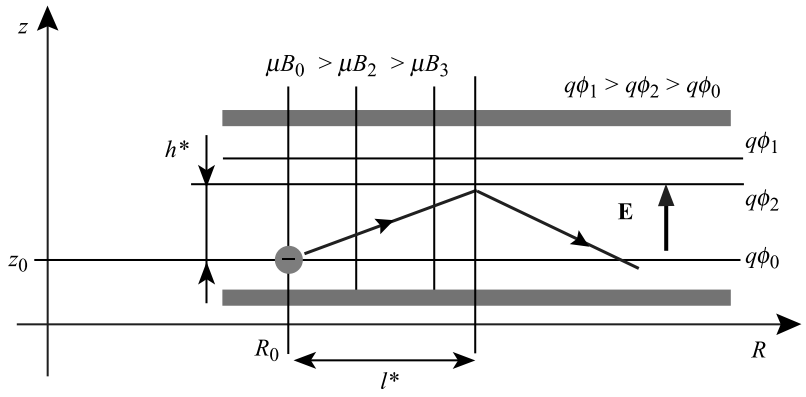

FIG. 9. A dynamical limitation of this DEC scheme: if a particle is allowed to move too far without striking an electrode, the energy transfer will reverse and the particle will start to take energy from the fields rather than transferring energy to the fields. Reversal of the energy transfer, resulting from the inertial/polarization drift, occurs at a point ($z - z_0 = h^*, R = R_0 + l^*$).

Thus, Eqs. (23) and (24) are replaced by

$$\frac{d\varepsilon_\parallel}{dt} = -\left[\left(\mathbf{v}_D + \mathbf{v}_{\mathrm{DI}} + v_\parallel \frac{\mathbf{B}}{B}\right)\cdot\nabla\right]\left(q\phi + \mu B + \frac{m}{2}\frac{E^2}{B^2}\right) \tag{52}$$

and

$$\frac{d\varepsilon_\perp}{dt} = \left[\left(\mathbf{v}_D + \mathbf{v}_{\mathrm{DI}} + v_\parallel \frac{\mathbf{B}}{B}\right)\cdot\nabla\right]\mu B \tag{53}$$

completed by the inertial/polarization drift effect

$$\frac{d\varepsilon_{E/B}}{dt} = \left[\left(\mathbf{v}_D + \mathbf{v}_{\mathrm{DI}} + v_\parallel \frac{\mathbf{B}}{B}\right)\cdot\nabla\right]\left(\frac{m}{2}\frac{E^2}{B^2}\right), \tag{54}$$

where

$$\left(\mathbf{v}_D + \mathbf{v}_{\mathrm{DI}} + v_\parallel \frac{\mathbf{B}}{B}\right)\cdot\nabla = \left(\frac{2\varepsilon_\parallel + \varepsilon_\perp}{qE\tau} - \frac{mE}{qB^2\tau}\right)\frac{\partial}{\partial z} + \frac{E}{B}\frac{\partial}{\partial R}, \tag{55}$$

rather than Eq. (25).

The evolution of the thermal parallel and perpendicular cyclotron energies fulfills

$$\frac{d\varepsilon_\parallel}{dt} = -\frac{2\varepsilon_\parallel}{\tau}, \tag{56}$$

$$\frac{d\varepsilon_\perp}{dt} = -\frac{\varepsilon_\perp}{\tau}. \tag{57}$$

Note that this $\varepsilon_\perp$ is the part of the kinetic energy in the Larmor gyration, not the total kinetic energy in the perpendicular direction (which also includes drift motion contribution $\varepsilon_{E/B}$). The evolution of $\varepsilon_{E/B}$ [Eq. (54)] is given by

$$\frac{d\varepsilon_{E/B}}{dt} = \frac{2\varepsilon_{E/B}}{\tau}. \tag{58}$$

It can be checked that Eqs. (51) and (48) are consistent with Eqs. (56)–(58) as $Ez = \phi$. Equations (56)–(58) can be integrated directly. The three components of the kinetic energy evolve, respectively, according to

$$\varepsilon_\parallel = \varepsilon_{\parallel 0}\exp\left(-\frac{2t}{\tau}\right), \tag{59}$$

$$\varepsilon_\perp = \varepsilon_{\perp 0}\exp\left(-\frac{t}{\tau}\right), \tag{60}$$

$$\varepsilon_{E/B} = \frac{\varepsilon_0}{2C}\exp\left(\frac{2t}{\tau}\right), \tag{61}$$

where we have defined the constant

$$C \doteq \frac{\varepsilon_0 B_0^2}{mE^2}. \tag{62}$$

The physical meaning of this important control parameter can be understood in more than one way. We can recast its definition as $(\varepsilon_0/mc^2)\times$ (magnetic energy density divided by electric energy density). For example, given a typical ratio $\varepsilon_0/mc^2 \approx 0.02$ and our targeting the value $C \approx 10$ requires a magnetic density of energy 500 times larger than the electric energy density. Alternatively, C can be understood in terms of the speed of a particle with kinetic energy ε_0 and the $\mathbf{E}\times\mathbf{B}$ velocity. If the speed of a particle with energy ε_0 is much faster than the drift velocity, then $C \gg 1$; if the drift is much faster, then $C \ll 1$.

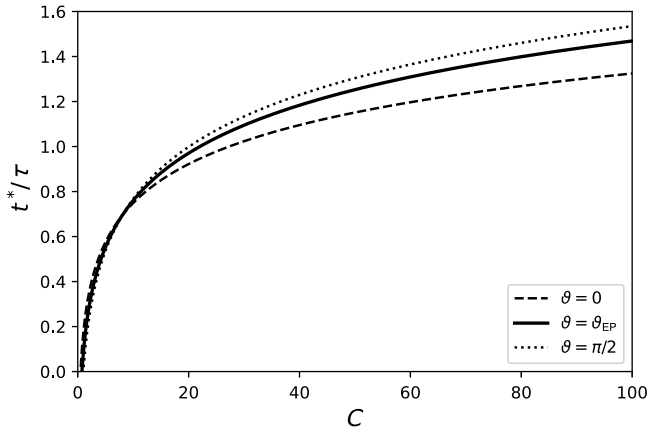

FIG. 10. Critical time t^* after which the energy transfer reverses as a function of the dimensionless parameter C. The curves shown here take $\vartheta = 0$, $\vartheta = \vartheta_{EP}$, and $\vartheta = \pi/2$, respectively.

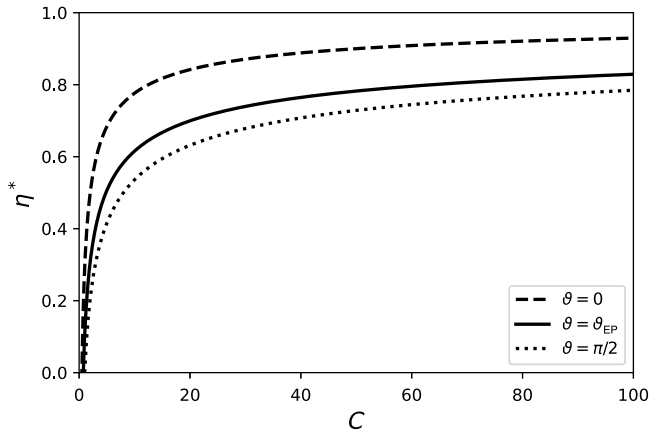

FIG. 11. Maximum free energy extraction efficiency as a function of the dimensionless parameter C for selected values of ϑ. This maximum takes into account dynamical but not geometrical constraints (i.e., it assumes there is an optimally large device).

The transfer of kinetic energy to potential energy is expressed as

$$qE(z - z_0) = \varepsilon_{\parallel 0}\left[1 - \exp\left(-\frac{2t}{\tau}\right)\right] + \varepsilon_{\perp 0}\left[1 - \exp\left(-\frac{t}{\tau}\right)\right] + \frac{mE^2}{2B_0^2}\left[1 - \exp\left(\frac{2t}{\tau}\right)\right]. \quad (63)$$

The key effect captured by the inclusion of $\mathbf{v}_{DI}$ is that the increase in $\mathbf{E} \times \mathbf{B}$ flow energy, as the particle moves outwards, tends to slow and eventually reverse the transfer from kinetic energy to potential energy.

The time t^* at which this reversal occurs is given by $dz/dt = 0$ in Eq. (48),

$$2\varepsilon_{\parallel}\left(t^*\right) + \varepsilon_{\perp}\left(t^*\right) = \frac{mE^2}{B^2} = \frac{mE^2}{B_0^2}\exp\left(\frac{2t^*}{\tau}\right), \quad (64)$$

so we have to solve

$$2C\cos^2\vartheta + C\sin^2\vartheta\exp\left(\frac{t^*}{\tau}\right) = \exp\left(\frac{4t^*}{\tau}\right) \quad (65)$$

to find t^*. Numerical solutions of Eq. (65) for the cases of $\vartheta = 0$, $\vartheta = \vartheta_{EP}$, and $\vartheta = \pi/2$ are shown in Fig. 10.

The logarithmic behavior of this numerical solution describing the initial equipartition case reflects the behavior of the particular solutions associated, respectively, with $\vartheta = 0$ and $\vartheta = \pi/2$:

$$\left.\frac{t^*}{\tau}\right|_{\vartheta=0} = \ln(2C)/4, \quad (66)$$

$$\left.\frac{t^*}{\tau}\right|_{\vartheta=\pi/2} = \ln(C)/3. \quad (67)$$

The maximum free energy extraction efficiency in a large device, free of the geometrical limitations analyzed in the previous section, is given by

$$\eta^*(E, B_0, \varepsilon_0, \vartheta) = 1 - \cos^2\vartheta\exp\left(-\frac{2t^*}{\tau}\right) - \sin^2\vartheta\exp\left(-\frac{t^*}{\tau}\right). \quad (68)$$

Numerical solutions for this maximum efficiency $\eta^*(C)$ for a large device are shown in Fig. 11 for the cases of $\vartheta = 0$, $\vartheta = \vartheta_{EP}$, and $\vartheta = \pi/2$. Figure 11 provides a description of the efficiency η^* as a function of the principal control parameter. On the basis of Fig. 11, we can conclude that the choice $C \sim 10$ is sufficient to reach a conversion efficiency on the order of 2/3, and a value on the order of approximately 50 makes it possible to convert about three quarters of the thermal energy into electric energy.

The algebraic behavior of the type $1 - \alpha C^{-\beta}$ of this numerical solution describing the initial equipartition case reflects the behavior of the particular solutions associated, respectively, with $\vartheta = 0$ and $\vartheta = \pi/2$:

$$\eta^*(\vartheta = 0) = 1 - C^{-1/2}/\sqrt{2}, \quad (69)$$

$$\eta^*(\vartheta = \pi/2) = 1 - C^{-1/3}. \quad (70)$$

The efficiency of a real device will depend on the birth distribution of charged particles both in $(\varepsilon_0, \vartheta)$ space and

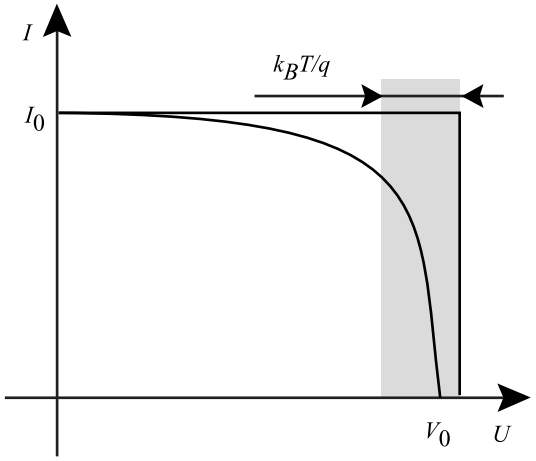

FIG. 12. The current-voltage characteristic for a DEC generator of this type is initially flat, with little dependence of the current on the voltage. At higher voltages, the output current drops as a function of the voltage.

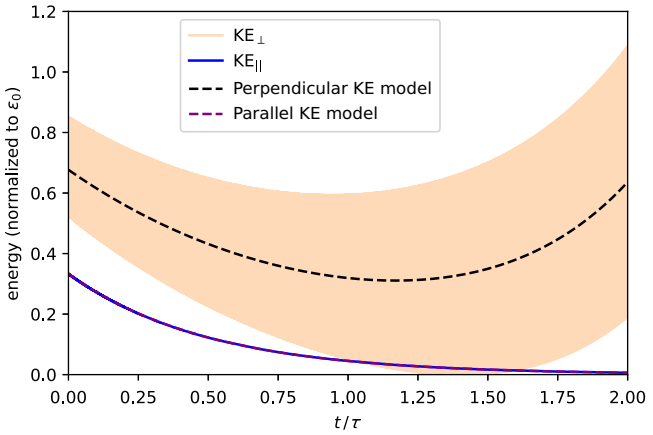

FIG. 13. Numerical validation of the analytic model using a single-particle simulation. This case had $C = 50$, from which we would expect a turning point at $t \approx 1.253\tau$. The region colored in by the perpendicular kinetic energy (KE) curve is the result of fast oscillations due to the gyrophase-dependent orientations of the Larmor motion and the drift motion.

in spatial position (z_0, R_0). For any birth distribution, it is clear that this effect will reduce the realizable efficiency. This can be understood as a limitation on the I-U curve describing the operation of an adiabatic DEC generator. The total voltage drop of the configuration can be increased by one either increasing E or increasing h. For any given starting condition $(\varepsilon_0, \vartheta)$, if either E or h is increased beyond some threshold, the particle will not reach the collection plate before its trajectory reverses. Note, however, that although increasing either E or h will increase the total voltage drop, and either will eventually cause electrons to turn before they reach the negative electrode, these two parameters influence the dynamics in different ways. E and h both change the total energy that must be extracted before a particle can traverse a given axial distance, but changing E also modifies the feedback from the inertial drift.

If all electrons reach the negatively charged electrode, then the total device current I is set by the rate of ionization events or the rate of incoming flow of charged particles, and I is independent of U. However, as U increases, there is a threshold (which will depend on the birth distribution of the charged particles and on the size, field strength, and shape of the configuration) where I will quickly drop off as a result of electrons turning before they can reach the negative electrode. Qualitatively, this will produce an I-U characteristic like the one pictured in Fig. 12, although one should keep in mind that the details of this curve will depend not only on the details of the birth distribution but also on what is held fixed when the voltage is increased. For any particular case, this curve makes it possible to determine the highest-power operating point; one can draw the set of isopower hyperbolae $IU = \text{const}$ and select the one that is tangent to the convex I-U generator characteristic.

In the most idealized case, in which the birth distribution is monoenergetic and all particles are born at the same spot and with the same ϑ, the I-U curve is a step function with constant $I = I_0$ for all $U < V_0$, and then $I = 0$ for all $U \geq V_0$ (with V_0 corresponding to the threshold at which the particles turn before reaching the boundary $dz/dt = 0$). In this case, the highest-power operating point corresponds to the corner of the I-U curve, with $P = I_0\, V_0$. For the case of a radiation-driven plasma generation, this power would be a linear function of the absorbed radiation (since this would determine the total number of ionization events). From Eq. (47), $dz/dt = 0$ implies that $mE^2/B^2 = \mathcal{O}(k_BT)$, so $V_0 = Eh = \mathcal{O}(B_0 v_{\text{th}} h)$, where v_{th} is the thermal velocity.

The previous analytic calculations can be validated numerically by means of single-particle simulations. Figure 13 shows one such example.

The simulation shown in Fig. 13 used a single-particle Boris pusher and had $C = 50$ and $\vartheta = \vartheta_{\text{EP}}$. Note that for these parameters, Eq. (65) can be solved numerically to yield $t^* \approx 1.253\tau$. This is consistent with the turning point seen in the simulation. The fluctuations in the numerically observed perpendicular kinetic energy for the model are the result of the gyrations of the particle. Depending on the gyrophase, the Larmor motion can have either positive or negative radial components.

The energy in the perpendicular motion can be decomposed into gyration energy and drift-motion energy on average. The kinetic energy used for the model in Fig. 13 includes both $\varepsilon_\perp$ and $mE^2/2B^2$.

These simulations confirm the validity of the previous analytic model and point toward the necessity to consider an additional possibility to convert the cyclotron energy into the parallel energy. We saw in Sec. IV that a gradient

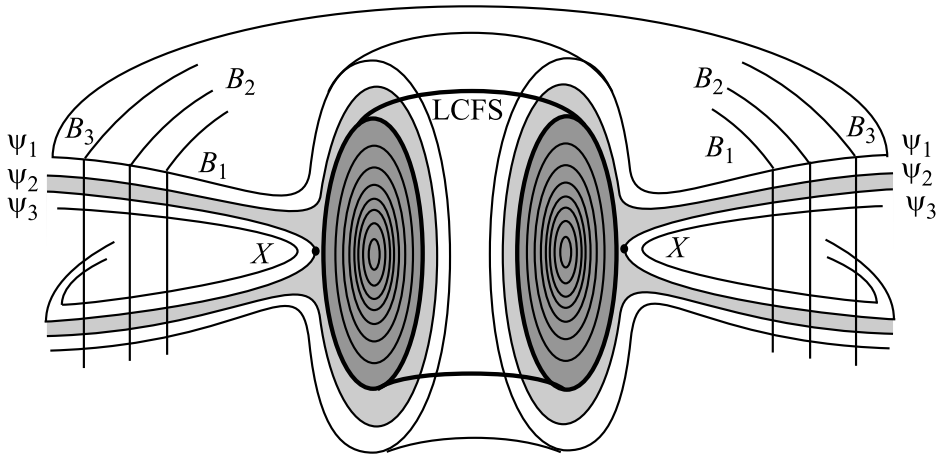

FIG. 14. Magnetic flux surfaces in a tokamak, with the last closed flux surface (LCFS) marked.

of the field strength along the field line offers such a possibility, and this optimization strategy will be explored in a forthcoming study.

VII. RADIATION FLUX AND PLASMA FLOW HEAT CONVERSION

In this section we briefly describe two types of adiabatic DEC implementation in ^{2}H-^{3}H tokamak reactors and in aneutronic p-^{11}B reactors.

In a tokamak reactor, the hot thermonuclear plasma diffuses from the confining closed field line to the open field lines of the divertor. The last closed flux surface defines the boundary of the confining toroidal configuration. The set of diverted field lines defines the open magnetic surfaces illustrated in Fig. 14.

Far from the X-point line, the magnetic field in the outer part of the divertor, illustrated in Fig. 14, is toroidal, and a dedicated set of upper and lower electrodes can polarize these magnetic surfaces such that they become also equipotential surfaces Ψ_1, Ψ_2, Ψ_3. The (B_i, Ψ_j) coordinates in Fig. 14 become similar to the $(\mu B_i, q\phi_j)$ energy coordinates in Fig. 8. The collecting plate can be matched to the upper and lower Ψ surfaces. In doing so, we have realized the geometry of a toroidal generator and we can envision extracting part of the free enthalpy of the divertor plasma flow in such a configuration. Lowering the temperature in the divertor before the ultimate plasma-solid material interaction is one of the main problems of tokamak physics; here this is achieved along with free enthalpy extraction. This geometry of an advanced divertor requires a far more detailed analysis, which is left to future work. This controlled cooling of the divertor plasma may also be beneficial to the core plasma inside the last closed flux surface as the control of the temperature gradient might help to make improved-confinement modes more accessible.

We now consider the case of rotating-mirror p-^{11}B reactors. Because of the high temperature, the thermonuclear plasma column is strongly radiating both in the microwave range, as a result of electron cyclotron/synchrotron emission, and in the UV-X range, as a result of electron bremsstrahlung. Keeping the axisymmetric geometry [Fig. 6(b)], we can design a conversion blanket all around this magnetized radiating plasma column, where the escaping intense radiation will ionize a vapor (e.g., cesium vapor) and heat the associated plasma. The escaping radiation can also be absorbed by metal target plates (e.g., tungsten plates), and the resulting hot metal plate can act as a hot electron source, whose energy is converted by the $\mathbf{E} \times \mathbf{B}$ poloidal configuration of the conversion blanket.

Various toroidal, poloidal, and mixed declinations of the $\mathbf{E} \times \mathbf{B}$ configurations can be adapted to both ^{2}H/^{3}H tokamak reactors and in aneutronic p-^{11}B reactors. The identification of the most relevant designs cannot be addressed on the basis of the simple discussion of this section, and is left for a future study.

VIII. CONCLUSION

We suggest a technique for converting power from plasma and radiation to electricity. A technology that could efficiently capture and convert power from plasma and radiation to electricity could be useful in a wide variety of applications. For example, magnetic confinement fusion typically involves heating plasmas to temperatures at which radiative losses can be significant. The ability to recapture this energy could be most critically important for reactors burning aneutronic fuels, which often require higher temperatures with correspondingly higher radiative losses. For instance, bremsstrahlung and synchrotron losses are a major hurdle for economical p-^{11}B fusion [23–26]. In very hot fusion plasmas, measures have been proposed to suppress this radiation primarily through plasma absorption and redirection to kinetic energy, as well as through suppression of the population of high-energy electrons [27–30]. However, the direct energy

conversion schemes here could, in principle, act synergistically with these other techniques. The manipulation of the plasma six-dimensional phase space has been recognized as necessary for making economical fusion through high-temperature aneutronic fusion approaches in general [31], and the techniques proposed here can be imagined working either separately or in concert with these phase space techniques.

For a hot plasma such that $k_B T \sim \varepsilon_0$, the design of a generator implies the choice of the geometrical characteristics (R_0, l, h) and of the field strengths (E, B_0). We have found that the various physical and geometrical constraints are functions of the two control parameters $\tau = B_0 R_0/E$ and $C = \varepsilon_0 B_0^2/mE^2$. The description of the poloidal-geometry dynamics requires a third control parameter, $\tau_0 = L\sqrt{2m\varepsilon_{\parallel 0}}/\varepsilon_{\perp 0}$. The poloidal geometry displays an additional advantage over the toroidal geometry as the cyclotron energy can be continuously converted into parallel energy. Such a possibility is advantageous because $\mathbf{E} \times \mathbf{B}$ configurations convert the parallel energy to dc electric power at a far faster rate than the cyclotron (perpendicular) energy. The design of an optimal field is clearly the next question to be addressed to identify efficient $\mathbf{E} \times \mathbf{B}$ conversion schemes for both ^{2}H-^{3}H tokamak and p-^{11}B advanced reactors.

The idea of poloidal and toroidal DEC rests on the tendency of the ∇B drift to carry particles in different directions depending on the sign of their charge. Its implementation in p-^{11}B advanced reactors relies on radiative ionization and heating. Radiation can deposit significant energy, after ionization, in the resulting ions and electrons.

Note that the transfers of energy considered here—for example, between kinetic energy and electric fields—are all adiabatic. This can be contrasted with work (such as the α-channeling concept [32]) that instead accomplishes this transfer using resonant interactions.

This adiabatic transfer process—like all energy conversion processes—will not be perfectly efficient. In this paper, we have considered two constraints on the performance of an adiabatic DEC device. The first is a matter of geometry: the charged particles need enough space to give up as much kinetic energy as possible before hitting a boundary of the device. Even in the absence of any other constraints, this is enough to prevent any realistic device from attaining perfect efficiency, since progressively greater efficiencies require exponentially increasing device sizes.

We also considered a dynamical constraint, wherein inertial drifts eventually slow (and subsequently reverse) the energy extraction process. The characteristic timescale involved depends on the parameter C. The highest efficiencies require higher values of C.

There are a variety of additional constraints and engineering challenges not considered here. For example, this kind of device relies on the presence of a large-enough population of neutral particles to absorb and be ionized by the incoming radiation. However, if that population were too large, collisions between charged and neutral particles would degrade the efficiency of the device.

In addition, a birth distribution of charged particles that is anything other than a δ function in r, z, ε_0, and ϑ will make it more difficult to efficiently tune the device parameters. For example, this would mean that different particles' trajectories would turn at different axial and radial positions.

However, these engineering challenges can likely be mitigated by careful control over the device geometry and the composition of the neutral population. The refinement and optimization of these ideas are planned for future work. Moreover, even relatively modest efficiencies could be an exciting development, particularly for applications in which the relevant radiation has wavelengths not amenable to other conversion techniques.

ACKNOWLEDGMENTS

This work was supported by ARPA-E Grant No. DE-AR0001554. J.-M.R. further acknowledges the hospitality of Princeton University and support from the Andlinger Center for Energy and the Environment through an Andlinger Center for Energy and the Environment fellowship, under which this work was initiated. E.J.K. acknowledges the support of the Department of Energy Fusion Energy Sciences Postdoctoral Research Program, administered by the Oak Ridge Institute for Science and Education and managed by Oak Ridge Associated Universities under Department of Energy Contract No. DE-SC0014664.

DATA AVAILABILITY

No data were created or analyzed in this study.

[1] E. A. Guggenheim, *Thermodynamics* (North Holland Publishing Company, Amsterdam, 1977).
[2] H. B. Callen, *Thermodynamics and an Introduction to Thermostatics* (John Wiley and Sons, New York, 1985).
[3] B. Sorensen, *Renewable Energy Conversion Transmission and Storage* (Academic Press, Amsterdam, 2007).
[4] R. Decher, *Energy Conversion Systems, Flow Physics and Engineering* (Oxford University Press, Oxford, 1994).
[5] I. I. Novikov, Efficiency of an atomic power generating installation, Sov. J. At. Energy **3**, 1269 (1957).
[6] P. Chambadal, *Les Centrales Nucléaires* (Armand Colin, Paris, 1957).
[7] F. L. Curzon and B. Ahlborn, Efficiency of a Carnot engine at maximum power output, Am. J. Phys. **43**, 22 (1975).
[8] J.-M. Rax, *Physique de la Conversion d'Énergie* (EDP Sciences, Les Ulis, France, 2012).

[9] G. W. Sutton, *Direct Energy Conversion* (McGraw-Hill Book Company, Paris, 1966).
[10] R. Decher, *Direct Energy Conversion Fundamentals of Electric Power Production* (Oxford University Press, Oxford, 1997).
[11] L. J. Perkins, G. H. Miley, and B. E. Logan, Novel fusion conversion methods, Nucl. Instrum. Methods Phys. Res. **A271**, 188 (1988).
[12] H. Takeno, K. Ichimura, S. Nakamoto, Y. Nakashima, H. Matsuura, J. Miyazawa, T. Goto, Y. Furuyama, and A. Taniike, Recent advancement of research on plasma direct energy, Plasma Fusion Res. **14**, 2405013 (2019).
[13] H. Momota, Y. Tomita, M. Ishikawa, and Y. Yasaka, A traveling wave direct energy converter for D-3HE fueled fusion reactor, Fusion Technol. **35**, 60 (1999).
[14] K. Yoshikawa, S. Kouda, Y. Yamamoto, and K. Maeda, Development of a two-dimensional particle trajectory code and application to a design of a plasma direct energy converter in the fusion engineering facility based on mirror plasma confinement, Fusion Technol. **14**, 264 (1988).
[15] V. I. Volosov, Recuperation of charged particle energy in traps with rotating plasma, Trans. Fusion Sci. Technol. **47**, 351 (2005).
[16] A. V. Timofeev, A scheme for direct conversion of plasma thermal energy into electrical energy, Fiz. Plazmy **4**, 351 (1978).
[17] S. Dushman, Electron emission from metals as a function of temperature, Phys. Rev. **21**, 623 (1923).
[18] G. N. Hatsopoulos and E. P. Gyftopoulos, *Thermionic Energy Conversion* (MIT Press, Cambridge, 1973).
[19] F. G. Balsht, G. A. Dyuzhev, A. M. Martsinovskiy, B. Y. Moyzhes, E. B. Sonin, and V. G. Yur'Yev, Thermionic converters and low-temperature plasma, Tech. Rep. (Technical Information Center, US-DoE, Washington, 1978).
[20] A. V. Nedospasov, The physics of MHD generators, Sov. Phys. Usp. **20**, 861 (1977).
[21] G. W. Sutton and A. Sherman, *Engineering Magnetohydrodynamics* (Dover Publication Inc, New York, 1965).
[22] R. J. Rosa, *Magnetohydrodynamic Energy Conversion* (McGraw-Hill Book Company, New York, 1968).
[23] S. V. Putvinski, D. D. Ryutov, and P. N. Yushmanov, Fusion reactivity of pB^{11} plasma revisited, Nucl. Fusion **59**, 076018 (2019).
[24] E. J. Kolmes, I. E. Ochs, and N. J. Fisch, Wave-supported hybrid fast-thermal p-^{11}B fusion, Phys. Plasmas **29**, 110701 (2022).
[25] I. E. Ochs, E. J. Kolmes, M. E. Mlodik, T. Rubin, and N. J. Fisch, Improving the feasibility of economical proton-boron-11 fusion via alpha channeling with a hybrid fast and thermal proton scheme, Phys. Rev. E **106**, 055215 (2022).
[26] I. E. Ochs and N. J. Fisch, Lowering the reactor breakeven requirements for proton–boron 11 fusion, Phys. Plasmas **31**, 012503 (2024).
[27] V. I. Volosov, Aneutronic fusion on the base of asymmetrical centrifugal trap, Nucl. Fusion **46**, 820 (2006).
[28] M. E. Mlodik, V. R. Munirov, T. Rubin, and N. J. Fisch, Sensitivity of synchrotron radiation to the superthermal electron population in mildly relativistic plasma, Phys. Plasmas **30**, 043301 (2023).
[29] V. R. Munirov and N. J. Fisch, Suppression of bremsstrahlung losses from relativistic plasma with energy cutoff, Phys. Rev. E **107**, 065205 (2023).
[30] I. E. Ochs and N. J. Fisch, Electron tail suppression and effective collisionality due to synchrotron emission and absorption in mildly relativistic plasmas, Phys. Plasmas **31**, 083303 (2024).
[31] H. Qin, Advanced fuel fusion, phase space engineering, and structure-preserving algorithms, Phys. Plasmas **31**, 050601 (2024).
[32] N. J. Fisch and J.-M. Rax, Interaction of energetic alpha particles with intense lower hybrid waves, Phys. Rev. Lett. **69**, 612 (1992).